HAL
open science

On the Numerical Modeling of Magnetoelectric device

Xavier Mininger, Hakeim Talleb, Thomas Henneron

To cite this version:

Xavier Mininger, Hakeim Talleb, Thomas Henneron. On the Numerical Modeling of Magnetoelectric device. International Compumag society Newsletters, 2016, 23 (3), pp.1026-0854. hal-01660582

HAL Id: hal-01660582

https://hal.sorbonne-universite.fr/hal-01660582

Submitted on 17 Mar 2020

HAL is a multi-disciplinary open access archive for the deposit and dissemination of scientific research documents, whether they are published or not. The documents may come from teaching and research institutions in France or abroad, or from public or private research centers.

L'archive ouverte pluridisciplinaire **HAL**, est destinée au dépôt et à la diffusion de documents scientifiques de niveau recherche, publiés ou non, émanant des établissements d'enseignement et de recherche français ou étrangers, des laboratoires publics ou privés.

On the Numerical Modeling of Magnetoelectric devices

X. Mininger[1], H. Talleb[2], T. Henneron [3]

[1]Group of electrical engineering-Paris (GeePs), CNRS UMR8507, CentraleSupelec, Univ Paris Sud, UPMC, Paris, France
[2]Sorbonne Universités, UPMC Univ Paris 06, UR2, L2E, Paris, France
[3]Université Lille1, Laboratory of electrical engineering and power electronics (L2EP), EA 2697, Villeneuve d'ascq, France

This paper describes the main stages of development of a numerical tool dedicated to the modeling of the magnetoelectric effect. The proposed approaches enable to take into account the nonlinearities of the material, a static and dynamic excitation and a transient state. The developed models are based on the finite element method in 2 or 3 D. To reduce the computation time of frequency-dependent numerical models, the Proper Generalized Decomposition, which is a Model Order Reduction method, is introduced. Each proposed model is illustrated with an application example. The presented work is based on the contributions of three French laboratories: GeePs, L2E and L2EP.

***Index Terms* — Magnetoelectric problem, Piezoelectricity, Magnetostriction, Finite element method, Proper generalized decomposition.**

I. Introduction

The Coupling of magnetic and electric quantities is naturally present with Maxwell equations considering displacement currents in Ampère's law and/or the derivative of the magnetic flux density in Faraday's law. Electromagnetic metamaterials also deal about a "magnetoelectric" coupling, obtained by instance when considering the effective behavior of a complex arrangement of electrically conductive elements [1]. The magnetoelectric (ME) effect described in this paper is however related to a "material" magnetoelectric coupling. This ME effect commonly refers to the modification of electric polarization of a material resulting from an applied magnetic field. The corresponding reverse effect is associated to the change of magnetization due to an applied electric field. This effect has been observed in single phase materials, but with relatively small interactions comparing to the one obtained when considering composite material. Such composites are commonly made with combinations of piezoelectric and magnetostrictive phases, and the "extrinsic" effect is related to both the magneto-mechanical and electro-mechanical couplings, see Fig. 1. The advantage of such structure is related to the resulting high magnetic and electric susceptibilities, as the ME effect is related to the product of the two quantities [2]. Two families of ME composites have been studied: particles of phase 1 placed in a matrix of phase 2, or laminate composites with the stacking of phase1/phase2 layers.

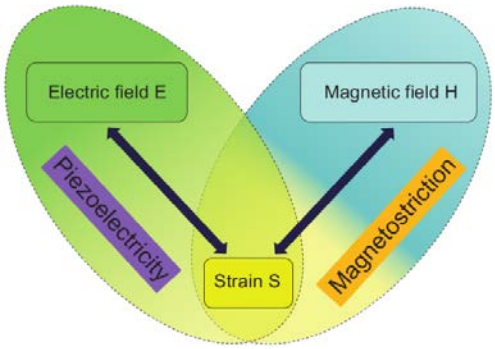

FIG. 1 Magnetoelectric effect for composite materials

Even if the ME effect still needs to be studied to consider its use in industrial applications, there is a wide range of potential ME devices, from magnetic sensors to storage devices [3]. As a consequence, the ME has been widely studied in the past decade, mainly in an experimental point of view [2]. Modeling approaches are more uncommon and often based on strong assumptions, especially when considering analytical studies [4]. The main modeling difficulty is related to the non-linearities associated to the magnetostrictive material, observed first in the magnetization curve and also for the strain dependence with the magnetic excitation. ME coupling has been studied in a "material" point of view, with homogenization techniques and the calculation of effective properties of a composite [5]. In order to study actual ME devices, the present paper summarizes the main steps of the development of a tool based on the finite element method and dedicated to the study of ME laminated devices. It has been developed with the contributions of three French laboratories: GeePs, L2E and L2EP. The paper focuses first on the development of the static and harmonic ME numerical models with the respective association of behavior laws/equilibrium equations. A second part deals with the consideration of the electric load associated to the ME device. Last part of the paper presents some recent results of model order reduction based on the Proper Generalized Decomposition in order to reduce the computation time of the ME modeling [17, 18, 19]. Devices based on the ME effect are detailed as we go along.

II. Magnetoelectric Effect with Static Excitation

A. *Magnetoelectric coupling in laminate composites*

A decade ago, experimental studies have shown that the association of piezoelectric and magnetostrictive materials led to higher ME interactions than the ones observed in single-phase materials [6]. A classic configuration was the magnetic field sensor obtained with stacks of different PZT and magnetostrictive layers, such as the examples proposed in Fig. 2. The working principle is as follows: the sensor is placed in a magnetic field, leading to the strain of the magnetostrictive

0018-9464 © 2015 IEEE. Personal use is permitted, but republication/redistribution requires IEEE permission.
See http://www.ieee.org/publications_standards/publications/rights/index.html for more information. (Inserted by IEEE.)

layer. The resulting strain of the PZT layers gives the electric polarization. The corresponding electric potential obtained on the electrodes gives the information of the measured magnetic field.

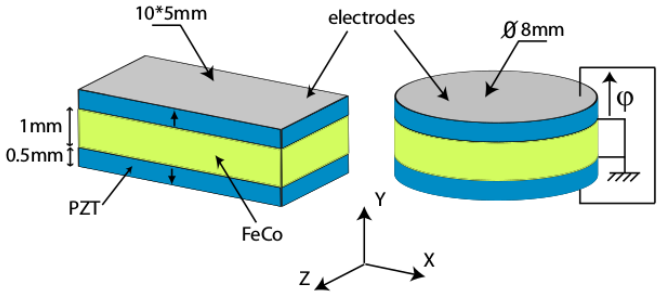

FIG. 2 FeCo(Green)/PZT(Blue) multilayers for magnetic field sensors based on ME effect

In order to propose an adequate numerical tool to evaluate such configuration, Galopin et al. [7] have first developed a finite element model that includes macroscopic constitutive laws of the materials, with the consideration of both magnetization and magnetostrictive non-linearities. The magnetostrictive non-linearity is introduced with the consideration of a magnetostriction strain s^{μ} that only depends on the magnetic flux density *b*. In such a case, the strain-stress relationship is expressed with Hooke's law:

$$t_{ij} = C_{ijkl}^{ms}\left(s_{kl} - s_{kl}^{\mu}\right) \tag{1}$$

where *s* is the total strain and C^{ms} the usual stiffness tensor. The model of $s^{\mu}(b)$ is a polynomial function that approximates the experimental curves of the magnetostriction strain obtained with a preliminary characterization step. The magnetic behavior law *h(b,s)* is deduced from integration of piezomagnetic coefficients over the strain, and is expressed with the magnetic field at free stress $h(b,s^{\mu})$ that also requests an experimental characterization:

$$h_i = h_i\left(b, s^{\mu}\right) - \frac{\partial t_{kl}^{\mu}}{\partial b_i}\left(s_{kl} - s_{kl}^{\mu}\right) \tag{2}$$

On the other side, the piezoelectric behavior only gives few difficulties: this material is considered with the standard linear equations, coupling the electric field *e* and the electric displacement field *d* to the mechanical quantities:

$$\begin{cases} t_{ij} = C_{ijkl}^{pz} s_{kl} - \alpha_{kij} e_k \\ d_i = \alpha_{ikl} s_{kl} + \varepsilon_{ij}^{s} e_j \end{cases} \tag{3}$$

Both constitutive laws are associated to magnetic and mechanical equilibrium equations considering static excitations:

$$\begin{cases} curl(h) = J \\ div(t) + f = 0 \end{cases} \tag{4}$$

with J the (optional) applied current density and f the body force.

B. FE Approach

Using the magnetic vector potential a, the mechanical displacement *u* and the electric potential *v*, the corresponding finite element formulation is based on the Galerkin method, associated with edge (if 3D) or nodal (if 2D) element discretization for magnetic degrees of freedom (DOF) and nodal discretization for mechanical and electrical DOF, and gives the following algebraic system:

$$\begin{cases} \left[K_{uu}^{s}\right](u) + \left[K_{up}^{s}\right](v) = (F) + \left(F^{mag}\right) + \left(F^{m}(b)\right) \\ -\left[K_{up}^{s}\right]^{t}(u) + \left[K_{pp}^{s}\right](v) = (Q) \\ \left[K_{aa}^{s}\right](a) = (J) + \left(J^{c}(b,s)\right) \end{cases} \tag{5}$$

where K_{aa}^{s} , K_{uu}^{s} and K_{pp}^{s} are respectively the magnetic, mechanical and electric stiffness matrix ('s' superscript is here for 'static'), K_{up}^{s} the piezoelectric matrix. *F*, F^{mag} and F^{m} are respectively nodal external, magnetic and "equivalent" magnetostriction forces; *Q* is the vector of nodal electric charges. $J^{c}(b,s)$ can be interpreted as a coercitive current density representing the effect of an applied stress. The resolution of this non-linear system is obtained with an iterative fixed-point method.

C. Applications

The numerical model has first been applied to the study of simple structures, such as the laminated ME devices presented in Fig. 2. Fig. 3 shows the resulting displacements for the cylindrical sensor. Due to the symmetries of the structure, only 1/8 of the 3D geometry is meshed. Using this numerical model, a comparison of the parallelepiped and cylindrical geometries has been proposed, and it has been shown that the obtained electric potential is greater with the parallelepiped solution, as presented in Fig. 4 [8].

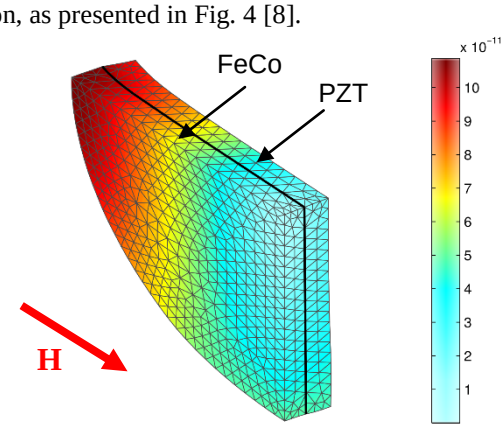

FIG. 3 Mechanical displacement for the cylindrical sensor (m)

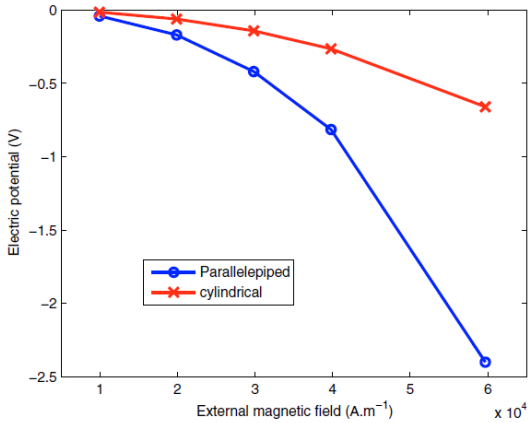

FIG. 4 Electric potentials versus external magnetic Field for the 2 ME sensor geometries

Thereafter, more complex devices have been considered, such as the displacement sensor proposed by Ueno, presented in Fig. 5 [7]. Its principle is to get an electric voltage on the piezoelectric electrodes depending on the position of a plate (not represented here) placed below the magnet. In this structure, the magnetic flux due to the magnet is derived between the mobile ferromagnetic plate and the Terfenol-D layer. Thereafter, small variations of the air gap between the magnet and the plate change the magnetic flux inside the magnetostrictive layer, which is associated to magnetostriction strain variation. This strain is then responsible for an electric field in the 2 PZT layers.

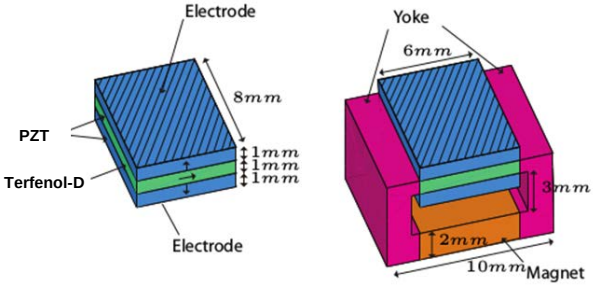

FIG. 5 Magnetoelectric displacements sensors

Different configurations have been studied with the static ME numerical model, depending on the pre-stress applied on the Terfenol-D layer, see Fig. 6. The simulated sensitivity seems to be in accordance with experimental measurement, especially in the free-stress case.

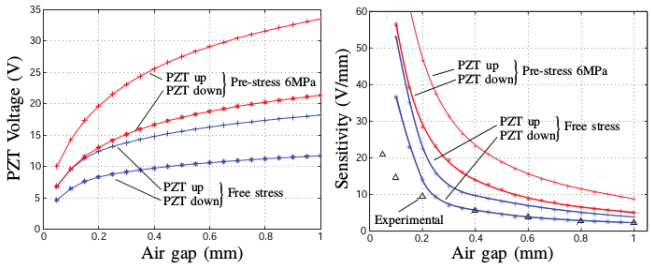

FIG. 6 Response of the magnetoelectric displacement sensor

Other devices have also been studied with the similar approach, such as magnetoelectric composites with interdigitated electrodes [9].

Although this first numerical model has proved its efficiency to consider the study of ME devices with *static* excitations, the increasing publication number in the last decade dealing with *harmonic* ME effect has shown the necessity of an upgrade of the numerical ME model.

III. Magnetoelectric Effect with Dynamic Excitation

A. Why do one introduce a dynamic excitation?

Even for the measurement of a static magnetic field, researchers have proposed to consider an additional harmonic component. The idea is to use the amplification of the structure displacements due to one of its mechanical resonance. Thus, even for a small harmonic excitation, the corresponding electric field will be largely greater than the one obtained with the static magnetic field only. If the system behavior was linear, a superimposition principle would apply, and only the electric response corresponding to the alternative component of the magnetic field would be amplified by the resonant effect. The response corresponding to the static magnetic field would only be amplified in an amount corresponding to the static magnetoelectric coefficient (see part II). As both magnetic and magnetostrictive show non-linear behavior, the static and resonant effects are coupled, and the magnetoelectric effect corresponding to the dynamic ME coefficient, enhanced through the resonance of the device, includes information on the static field. As a consequence, the model has to consider both the static and harmonic excitations, the second being considered small compared to the first one. A first numerical approach has been proposed in [9], showing the dependence between static and dynamic quantities. The following part details the method developed by [10] so as to include both static and dynamic simulations in the ME modeling.

B. Impact on equilibrium equations and behavior laws

The dynamic excitation is considered to be a sinusoidal signal, and the numerical model is then upgraded so as to include a harmonic part.

First, the mechanical equilibrium equation used in the model is modified in order to consider vibration modes:

$$div(t) + f = -\rho(2\pi f)^2 u \tag{6}$$

with ρ the mass density and f the frequency of the dynamic excitation. Depending on the frequencies and geometry of the considered application, eddy currents can be included or not in the model. When the skin depth calculated from analytical equation is much higher than the usual depth of magnetostrictive layers, magnetic equilibrium equation is the same as in the static study. On the other hand, the conductivity of the magnetostrictive material can be included in the model with usual approaches.

The second improvement represents a more innovative

challenge: the differentials of behavior laws (1) and (2) are calculated in order to describe a 'harmonic' constitutive laws around a polarization point of the magnetostrictive material (small signal problem, represented with the ~ sign) :

$$\begin{cases} \tilde{t}_{ij} = C^{ms}_{ijkl}\tilde{s}_{kl} - \dfrac{\partial t^{\mu}_{ij}}{\partial b_k}\tilde{b}_k \\ \tilde{h}_i = -\dfrac{\partial t^{\mu}_{kl}}{\partial b_i}\tilde{s}_{kl} + \left[\nu_{ij} - \dfrac{\partial^2 t^{\mu}_{kl}}{\partial b_i \partial b_j}\left(s_{kl} - s^{\mu}_{kl}\right) + \dfrac{\partial t^{\mu}_{kl}}{\partial b_i}\dfrac{\partial s^{\mu}_{kl}}{\partial b_j} \right]\tilde{b}_j \end{cases} \quad (7)$$

The terms in square bracket of the 2nd equation represent an equivalent reluctivity $\tilde{\nu}_{ij}$ that will be locally evaluated depending on the polarization imposed by the static excitation. Likewise, the magneto-mechanical coupling term is deduced from the considered polarization. Details on the calculation of these terms can be found in [11].

C. *Finite Element Approach*

Based on the equilibrium equations and "dynamic" behavior laws, the corresponding finite element model is obtained with the same approach than in the static case. The system solved in the dynamic case is the following:

$$\begin{cases} [K_{uu}](\tilde{u}) + [K_{up}](\tilde{v}) + [K_{ua}](\tilde{a}) = 0 \\ [K_{pu}](\tilde{u}) + [K_{pp}](\tilde{v}) = 0 \\ [K_{au}](\tilde{u}) + [K_{aa}](\tilde{a}) = (\tilde{J}) \end{cases} \quad (8)$$

K_{uu} includes here the 'static' mechanical stiffness matrix K^{s}_{uu}, but also the dynamic part with the mass matrix and a damping term. Piezoelectric, piezomagnetic and electric matrices are identical to the ones of the static model, unlike the magnetic one, because of the 'small signal' magnetostrictive behavior (7). Depending on the considered problem, the excitation at the frequency of a mechanical resonance can be a small dynamic current $(\tilde{J})$ or a small magnetic field h_{ac} imposed with Dirichlet conditions on the magnetic vector potential $\tilde{a}$ in the boundaries of the problem domain.

Finally, the global model includes both a static –to get the polarization quantities– and a dynamic –to evaluate the ME coefficient– calculations and the approach can be summarized with Fig. 7.

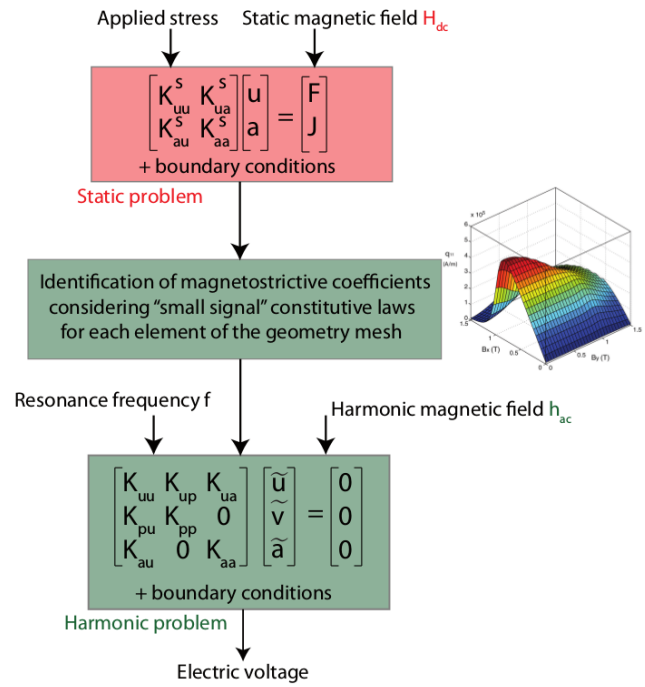

FIG. 7 Modeling procedure adapted to dynamic ME coefficient evaluation

The model has been first validated on some simple devices, such as the one presented in Fig. 8, by comparison with experimental studies. Fig. 9 shows the resulting 'dynamic' electric voltage obtained vs the applied 'static' magnetic field H_{dc} that has to be measured. The curve shows clearly a linear part, the electric voltage being proportional to the static magnetic field for small excitations.

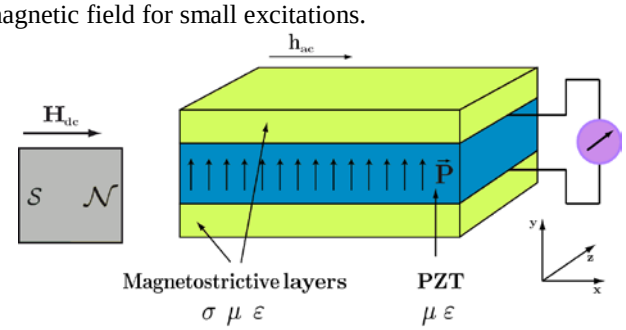

FIG. 8 Magnetic sensor configuration for dynamic ME effect

For higher magnetic fields, the electric voltage decreases: this effect is mainly related to the evolution of the coupling coefficient in the magnetostrictive behavior law (7). Indeed, the derivative of t^{μ} decreases to zero for high magnetic fields, as shown with the curve represented at the right part of Fig. 9. This evolution is in good accordance with the experimental results observed in [12].

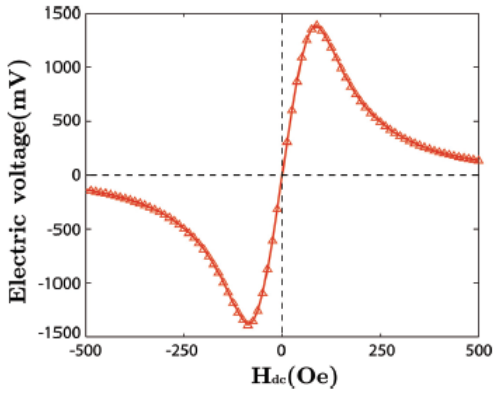

FIG. 9 Evolution of the dynamic electric field vs the static magnetic field H_{dc}

D. *Applications*

Other interesting ME devices are based on this combination of static and dynamic contributions. One can by instance get a tunable inductor, whose geometry looks similar to the previous magnetic sensor (Fig. 10) but with only very thin magnetostrictive layers of Metglas (23 µm). The main advantage of such solution comparing to classical tunable inductor is that it can easily be controlled with an applied static electric field E_{dc}. This electric field applied between the electrodes of the PZT layers introduces a deformation of the PZT, and the associated stress in the Metglas layer leads to a modification of the equivalent reluctivity $\tilde{\nu}_{ij}$ for this material, as presented in Eq. 7.

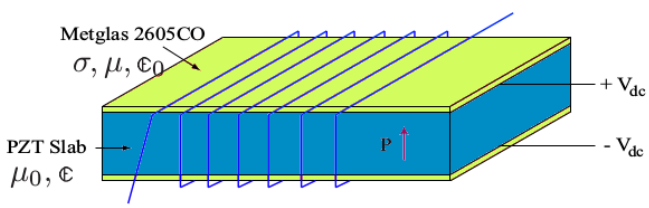

FIG. 10 Tunable magnetoelectric inductor

The proposed model is then adapted to first evaluate the stress in the magnetostrictive layer due to the static electric field E_{dc} (polarization point). The second part dealing with the dynamic excitation –the sinusoidal current injected in the coil– is however exactly the same than the one presented previously. The inductance is then evaluated with an energy approach for different static electric fields and different current frequencies. Modeling results presented in Fig. 11 show the two observations made by experimental researchers [13]: first, the decrease of E_{dc} gives increasing inductance values, and secondly the inductance is decreased for high current frequencies, as expected with the influence of the skin effect.

For some other applications, such as energy transducers, one need to consider a load associated to the piezoelectric layer. The next part details the corresponding numerical model.

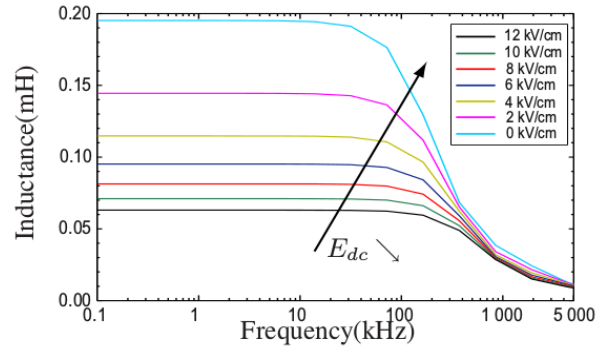

FIG. 11 Inductance vs frequency for different static electric fields E_{dc}

IV. Coupling with Electrical Load Equation

Since the piezoelectric layer is dielectric, there is no free charge inside it. All the free charges are confined to the electrodes. The current I flowing toward the electrical impedance load is the time derivative of the total electric charge Q, $I = \partial_t Q$, or $I = j\omega Q$ in harmonic regime.

In harmonic regime the terminal voltage of the load Z (resistive, capacitive or inductive) is given by ZI and is related to the voltage U between the electrodes by $U = ZI$. We can introduce an incident matrix K_{qp} that links the electrical potentials of electrodes of the piezoelectric layer and the voltage U. The unknown electric charge Q satisfies in harmonic regime the following condition:

$$VK_{qp} - jZ\omega Q = 0 \tag{9}$$

where the elements of K_{qp} are respectively equal to 1 or -1 if a node is associated with the top electrode or the bottom electrode, otherwise its elements are equal to 0.

In 2D assumption, the width L_z in the z-direction is not taking into account. Actually, this width is considered as normalized in according to [1m]. The current flowing toward the electrical impedance I is thus proportional of the surface $\mathcal{S} = L_x \times [1m]$ of the electrodes since $Q = CV$, where C is the capacitance between the electrodes of the piezoelectric given by:

$$C = \frac{\varepsilon^S \mathcal{S}}{t_p} \tag{10}$$

For a considered distance L_x, the capacitance C is then normalized as:

$$\bar{C} = \frac{C}{L_x} = \frac{\varepsilon^S \mathcal{S}}{t_p\, L_x} \tag{11}$$

In this case, the current I is also normalized by $\bar{I} = \partial_t\{\bar{C}V\} = \partial_t\left\{\frac{C}{L_x}V\right\} = \frac{I}{L_x}$. To conserve the physical quantity $V = ZI = Z\partial_t\{CV\}$, it is necessary to normalize also the

impedance Z by $\bar{Z} = ZL_x$.

$$V = \bar{Z}\bar{I} = ZL_x \frac{I}{L_x} = ZI \tag{12}$$

In considering a small signal harmonic ac field h_{ac} around a magnetization point H_{dc}, the coupling system equation (13) including the load equation can be solved in harmonic regime:

$$[\mathbb{K}]\{\mathcal{X}\} = \{\mathcal{F}\} \tag{13}$$

where $[\mathbb{K}]$ denotes the small signal linear matrix around a magnetization point. The terms in (13) have the form:

$$[\mathbb{K}] = \begin{bmatrix} K_{uu} - \omega^2 M + j\omega C_{uu} & K_{up} & 0 & K_{ua} \\ K_{pu} & K_{pp} & K_{pq} & 0 \\ 0 & K_{qp} & -j\omega\bar{Z} & 0 \\ K_{au} & 0 & 0 & K_{aa} \end{bmatrix}, \mathcal{X} = \begin{bmatrix} \tilde{\boldsymbol{u}} \\ \tilde{V} \\ \tilde{Q} \\ \tilde{a}_z \end{bmatrix}, \mathcal{F} = \begin{bmatrix} 0 \\ 0 \\ 0 \\ 0 \end{bmatrix} \tag{14}$$

As mentioned previously, the magnetic excitation is implemented in considering the Dirichlet conditions on the magnetic vector potential $\tilde{a}_z$ in the boundaries of the problem domain (Fig. 12).

The piezomagnetic coefficients and the permeability in K_{ua} and K_{aa} are incremental and determined by nonlinear solution on static regime under the magnetic bias H_{dc}, as developed in the previous part [10].

In transient regime, the electrical circuit equation depends on the natural of the electrical load. In the case of resistive load for example, we have $VK_{pq} - R\dot{Q} = 0$. The system to be solved takes the following form [14]:

$$[\mathcal{M}]\{\ddot{\mathcal{X}}\} + [\mathcal{C}]\{\dot{\mathcal{X}}\} + [\mathcal{K}]\{\mathcal{X}\} = [\mathcal{F}] \tag{15}$$

with,

$$[\mathcal{K}] = \begin{bmatrix} K_{uu} & K_{up} & 0 & K_{ua} \\ K_{pu} & K_{pp} & K_{pq} & 0 \\ 0 & K_{qp} & 0 & 0 \\ K_{au} & 0 & 0 & K_{aa} \end{bmatrix}, [\mathcal{C}] = \begin{bmatrix} C_{uu} & 0 & 0 & 0 \\ 0 & 0 & 0 & 0 \\ 0 & 0 & R & 0 \\ 0 & 0 & 0 & 0 \end{bmatrix}$$

$$[\mathcal{M}] = M, \mathcal{X} = [\boldsymbol{u} \quad V \quad Q \quad a]^T, \mathcal{F} = [0 \quad 0 \quad 0 \quad 0]^T$$

Again in the small signal assumption, the system equation is linear and has to be solved with a given time discretization scheme.

V. Example of a ME Energy Transducer

Although ME Composite structures can be considered for quasi-static energy harvesting [15], the model detailed in the previous part is here applied for a dynamic energy transducer. The studied example presented in Fig. 12 consists of an energy transducer composed of a trilayer Terfenol-D/PZT/Terfenol-D laminated composite. The device has the following dimensions: L_x=14mm, L_y=3mm (t_m=t_p=1mm). The excitation is an externally applied magnetic field H_{ext}.

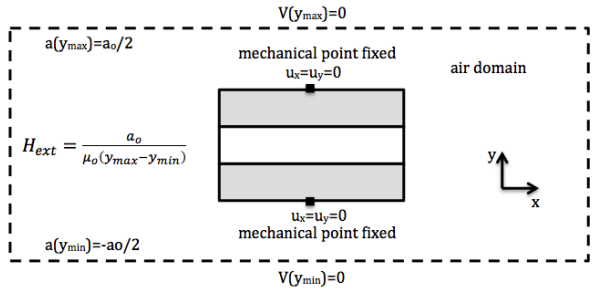

FIG. 12 Magnetic, electric and elastic boundary conditions

The solution domain includes an air domain around the composite and is illustrated in Fig. 12, where the magnetic, electric and elastic boundary conditions are, respectively, indicated. In particular, the constant magnetic vector potentials $a = \pm a_0/2$ with $a_0 = H_{ext}\mu_0(y_{max} - y_{min})$ are applied on the top and the bottom limits of the domain to take into account the externally applied magnetic field. The fixed mechanical displacements are here imposed on the middle of the composite, and the Dirichlet condition for the electric scalar potential is applied on the external boundary. The plane stress condition has been applied for 2D elastic problem:

$$t_{xx} = t_{xz} = t_{yz} = 0 \tag{16}$$

$$s_{xz} = s_{yz} = 0 \tag{17}$$

$$s_{xx} = -\vartheta(t_{xx} + t_{yy})/\mathfrak{E} \tag{18}$$

where $\mathfrak{E}$ and ϑ are respectively the Young's module and the Poisson coefficient that are related to the compliance constants by $\mathfrak{E} = \frac{1}{s_{11}}$ and $\vartheta = -\frac{s_{12}}{s_{11}}$

VI. Harmonic Regime Results

Fig. 13 shows the frequency dependence of the voltage coefficient $\tilde{\alpha}_V = V/h_{ac}$ under the various electrical loads R. The ME composite resonates under the open-circuit condition with $\tilde{\alpha}_{VMAX}$ close to *10 V/Oe*. This value is obtained with the viscous damping coefficients $\alpha = 0$, β=1.5x10^{-8}.

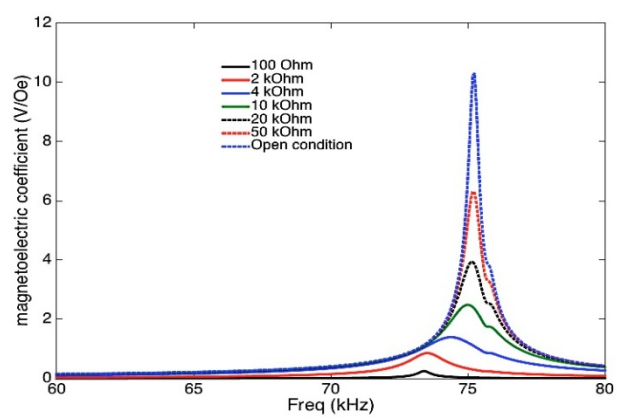

FIG. 13 $\tilde{\alpha}_V$ in function of frequency under different resistive loads

Fig. 14 shows the output deliverable power as function of the load resistance under different dc bias field. Finally under a dc bias field H_{dc} of 200Oe and an ac field h_{ac}=1Oe, a deliverable maximal power of 0.45 mW is obtained under a electrical load of 35 kOhm.

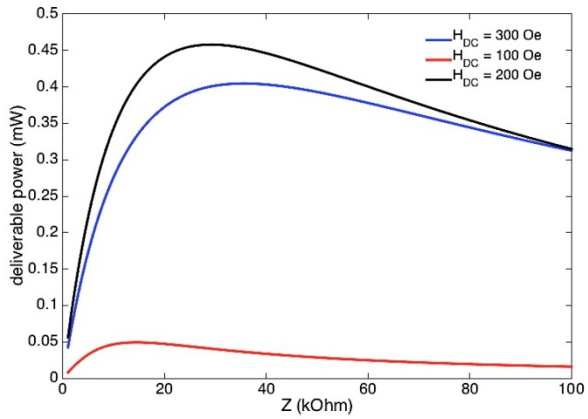

FIG. 14 Output deliverable power as function of the load resistance under different dc bias field

VII. Transient Analysis

The harmonic regime works with the assumption of small signal and linear material. However in the case of nonlinear materials or nonlinear signals the transient analysis becomes necessary to predict the energy transfer. This is by instance the case when the synchronized switch damping technique (SSD) is employed [15][16]. The use of a magneto-elastic-electric equivalent circuit model presented is possible but in contrast to the FEM, the model does not take into account rigorously the mechanical and electrical impacts when the structure is loaded by electrical impedance.

In our work, the Newmark method is employed to calculate the transient dynamic response [17]:

$$[\overline{K}]\{\mathcal{X}_{t+\Delta t}\} = \{R_{t+\Delta t}\} \text{ with } [\overline{K}] = [\mathcal{M}] + \Delta t a[\mathcal{C}] + \frac{\Delta t^2 b}{2}[\mathcal{K}] \quad (19)$$

where

$$\{R_{t+\Delta t}\} = \frac{\Delta t^2}{2} b\{\mathcal{F}_{t+\Delta t}\} + [\mathcal{M}]\left(\{\mathcal{X}_t\} + \Delta t\{\dot{\mathcal{X}}_t\} + \frac{\Delta t^2}{2}(1-b)\{\ddot{\mathcal{X}}_t\}\right) + [\mathcal{C}]\left(\Delta t a\{\mathcal{X}_t\} + \frac{\Delta t^2}{2}(2a-b)\{\dot{\mathcal{X}}_t\} + \frac{\Delta t^3}{2}(a-b)\{\ddot{\mathcal{X}}_t\}\right)$$

with $\{\ddot{\mathcal{X}}_{t+\Delta t}\} = \frac{2}{b\Delta t^2}(\{\mathcal{X}_{t+\Delta t}\} - \{\mathcal{X}_{\Delta t}\}) - \frac{2}{b\Delta t}\{\dot{\mathcal{X}}_{\Delta t}\} - \left(\frac{1}{b} - 1\right)\{\ddot{\mathcal{X}}_{\Delta t}\}$

$$\{\dot{\mathcal{X}}_{t+\Delta t}\} = \{\dot{\mathcal{X}}_{\Delta t}\} + \Delta t\left((1-a)\{\ddot{\mathcal{X}}_{\Delta t}\} + a\{\ddot{\mathcal{X}}_{t+\Delta t}\}\right),\ a = 1,\ b = \frac{1}{2}\left(a + \frac{1}{2}\right)^2$$

The principle of SSD technique is considered with the energy equilibrium of the system. Indeed, in considering the system (15) in open electric condition we can write the system:

$$\begin{cases} M\ddot{\tilde{u}} + C_{uu}\dot{\tilde{u}} + K_{uu}\tilde{u} + K_{up}\tilde{V} + K_{ua}\tilde{a}_z = 0 \\ K_{pu}\tilde{u} + K_{pp}V = 0 \\ K_{au}\tilde{u} + K_{aa}\tilde{a}_z = 0 \end{cases} \quad (20)$$

Thus, in combining the expression of $\tilde{a}_z = -{K_{aa}}^{-1}K_{au}u$ with $\tilde{u} = -{K_{pu}}^{-1}K_{pp}V$ in the first equation we obtain the equivalent system:

$$M\ddot{\tilde{u}} + C_{uu}\dot{\tilde{u}} + K_{uu}\tilde{u} + \left(K_{up} + \overline{K_{up}}\right)\tilde{V} = 0 \quad (21)$$

with $\overline{K_{up}} = K_{ua}{K_{aa}}^{-1}K_{au}{K_{pu}}^{-1}K_{pp}$.

The energy equilibrium can be obtained in multiplying both sides of Eq. (21) by the displacement velocity $\dot{\boldsymbol{u}}$ and integrating over the time variable:

$$\int_o^t M\ddot{\tilde{u}}\dot{\tilde{u}}\,dt + \int_o^t C_{uu}\dot{\tilde{u}}^2\,dt + \int_o^t K_{uu}\tilde{u}\dot{\tilde{u}}\,dt + \int_o^t\left(K_{up} + \overline{K_{up}}\right)\tilde{V}\dot{\tilde{u}}\,dt = 0 \quad (22)$$

The provided energy (22) is distributed into the kinetic energy $\frac{1}{2}M\dot{\tilde{u}}^2(t)$, potential elastic energy $\frac{1}{2}K_{uu}\tilde{u}^2(t)$, the mechanical damping $\int_o^t C_{uu}\dot{\tilde{u}}^2$ dt and the transmitted energy $\int_o^t\left(K_{up} + \overline{K_{up}}\right)\tilde{V}\dot{\tilde{u}}\,dt$ quantity. This latter corresponds to the mechanical energy, which is converted into electrical energy.

$$\int_o^t\left(K_{up} + \overline{K_{up}}\right)\tilde{V}\dot{\tilde{u}}\,dt = \frac{1}{2}C_o\tilde{V}^2 + \int_o^t \tilde{V}I\,dt \quad (23)$$

Thus, the maximization of this energy leads to minimization of the mechanical energy in the structure. The usefulness of a SSD control approaches is to maximize this energy in putting the voltage and displacement velocity in phase.

Several techniques exist, including one that imposes an inductance as the Synchronized Switch Damping on Inductor (SSDI) technique presented in Fig. 15. The switch is open, except when zero displacement velocities $\dot{\boldsymbol{u}}_{t+\Delta t}$ occur. At this instant, the switch is closed in a very short period that puts in phase the output voltage and displacement velocity. In this short period $t_i = \pi\sqrt{LC_o}$ the clamped capacitor C_o and the added inductance L (1nH here) represents an oscillator [15].

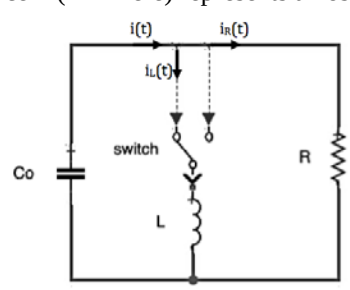

(a)

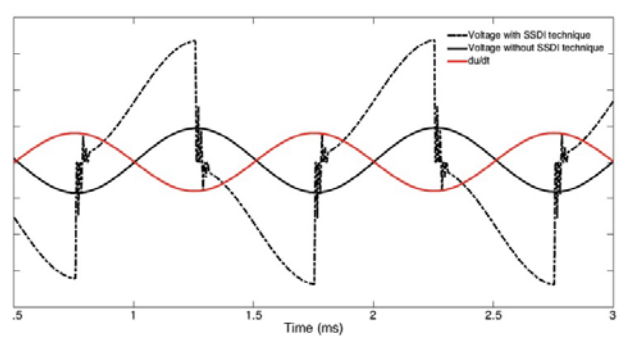

(b)

FIG. 15 SSDI nonlinear device and voltage and displacement velocity waveforms

To model the SSDI technique in the FEM multiphysic model, the current equation $i(t) = i_R(t) + i_L(t)$ has to be introduced in the transient system (15):

$$\partial_t i = \frac{\partial_t U}{R} + \frac{U}{L} \tag{24}$$

$$L\ddot{\tilde{Q}} - \frac{L}{R}\dot{\tilde{V}}K_{pq} - \tilde{V}K_{pq} = 0 \tag{25}$$

Accordingly, as shown in Fig. 16, when the SSDI harvesting technique is activated (i.e. time > 0.13ms) the output voltage reaches a maximal value and decreases until a steady state and the deliverable energy stored in the load $\int VIdt$ is strongly gradually increased.

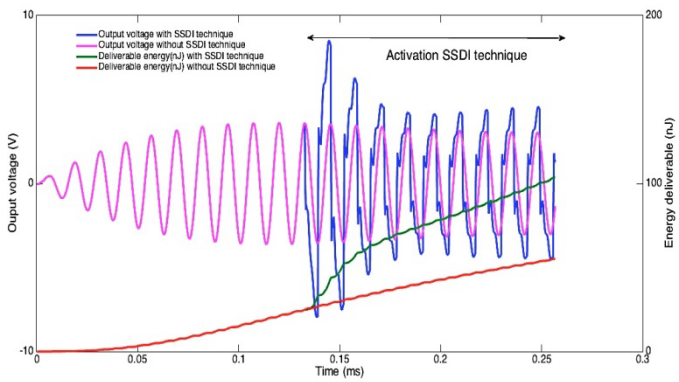

FIG. 16 Output voltage and deliverable energy transient response

VIII. Model Order Reduction Based on Proper Generalized Decomposition

To reduce the computation time of frequency-dependent numerical models, Model Order Reduction (MOR) methods have been developed and presented in the literature. These methods consist in searching a solution in a subspace of the approximation space of the full numerical model. They have been mainly used to solve problems in mechanics. In this field, the Proper Generalized Decomposition method has been developed since the early 2000's and knows an increasing interest in the scientific community [18, 19, 20]. In computational electromagnetics, the PGD approach has been developed to study a fuel cell polymeric membrane model [21]. In static electromagnetism, the nonlinear behavior of a Soft Magnetic Composite Material and of a three phase transformer has been modeled [22][23]. In the case of magneto-quasistatics, the skin effect in a rectangular slot or in a conducting plate has been addressed [24][25]. A squirrel cage induction machine at standstill and a magneto-thermal devices have been also studied [26][27]. In [28], a piezoelectric energy harvester is modeled. Then, we propose in the following part to apply the PGD approach with the magnetoelectric problem.

A. PGD formulation

To apply the PGD approach, we consider a weak formulation on $D\times[\omega_{\min}:\omega_{\max}]$ of the problem defined on the section III. Then, we have:

$$\int_{\omega_{min}}^{\omega_{max}}\int_D \boldsymbol{u}'(\boldsymbol{x})\cdot\left[div\boldsymbol{t}(\boldsymbol{x},\omega)+\rho\omega^2\boldsymbol{u}(\boldsymbol{x},\omega)\right]dDd\omega=0 \tag{26}$$

$$\int_{\omega_{min}}^{\omega_{max}}\int_D v'(\boldsymbol{x})\cdot div\boldsymbol{d}(\boldsymbol{x},\omega)dDd\omega=0 \tag{27}$$

$$\int_{\omega_{min}}^{\omega_{max}}\int_D a'(\boldsymbol{x})\cdot curl\boldsymbol{h}(\boldsymbol{x},\omega)dDd\omega=0 \tag{28}$$

The PGD method consists in approximating the solutions by sums of separable functions in frequency and space, so-called modes. Then, the electric potential, the magnetic potential and the mechanical displacement are approximated by separated representations of space and frequency functions,

$$v(\boldsymbol{x},\omega)\approx\sum_{j=1}^{M}R_j^v(\boldsymbol{x})S_j^v(\omega) \tag{29}$$

$$a_3(\boldsymbol{x},\omega)\approx\sum_{j=1}^{M}R_j^a(\boldsymbol{x})S_j^a(\omega) \tag{30}$$

$$\boldsymbol{u}(\boldsymbol{x},\omega)\approx\sum_{j=1}^{M}\boldsymbol{R}_j^u(\boldsymbol{x})S_j^u(\omega) \tag{31}$$

with $\boldsymbol{x}\in D$, $\omega\in[\omega_{\min}:\omega_{\max}]$ and M the number of modes of the expansions. To compute the set of functions $R_j^l(\boldsymbol{x})$ and $S_j^l(\omega)$ for $j\in[1:M]$ and $l=\{v, a, u\}$, an iterative enrichment approach is used. At the nth iteration, the functions $R_n^l(\boldsymbol{x})$ and $S_n^l(\omega)$ are computed with respect to the previous functions $R_i^l(\boldsymbol{x})$ and $S_i^l(\omega)$ with $i\in[1:n-1]$. To calculate $R_n^l(\boldsymbol{x})$ and $S_n^l(\omega)$, two sets of equation are solved iteratively.

In a first step, we assume that the functions $S_n^l(\omega)$ with $l=\{v, a, u\}$ are known. Then, the test functions in equations (26), (27) and (28) are $v'=R^{v\prime}(\boldsymbol{x})S_n^v(\omega)$, $a'=R^{a\prime}(\boldsymbol{x})S_n^a(\omega)$ and $\boldsymbol{u}'=\boldsymbol{R}^{u\prime}(\boldsymbol{x})S_n^u(\omega)$ with $R^{v\prime}(\boldsymbol{x})$, $R^{a\prime}(\boldsymbol{x})$ and $\boldsymbol{R}^{u\prime}(\boldsymbol{x})$ test functions defined on the same spaces of $R_n^v(\boldsymbol{x})$, $R_n^a(\boldsymbol{x})$ and $\boldsymbol{R}_n^u(\boldsymbol{x})$ respectively. In term of 2D discretisation, these functions are supported by the nodal shape functions. Then, we denote by $\boldsymbol{R}_n^u$, $\boldsymbol{R}_n^v$ and $\boldsymbol{R}_n^a$ the values on the Degrees of Fredoom of the functions $\boldsymbol{R}_n^u(\boldsymbol{x})$, $R_n^v(\boldsymbol{x})$ and $R_n^a(\boldsymbol{x})$ respectively. Finally, the system to be solved is:

$$\begin{bmatrix}\beta_{1,n}K_{uu}-\beta_{2,n}M+\beta_{3,n}C_{uu} & \beta_{4,n}K_{up} & \beta_{5,n}K_{ua}\\ \beta_{6,n}K_{pu} & \beta_{7,n}K_{pp} & 0\\ \beta_{8,n}K_{au} & 0 & \beta_{9,n}K_{aa}\end{bmatrix}\begin{bmatrix}\boldsymbol{R}_n^u\\ \boldsymbol{R}_n^v\\ \boldsymbol{R}_n^a\end{bmatrix}=\begin{bmatrix}0\\0\\ \beta_s\boldsymbol{F}_a\end{bmatrix}+$$

$$\sum_{i=1}^{n-1}\begin{bmatrix}\beta_{1,i}K_{uu}-\beta_{2,i}M+\beta_{3,i}C_{uu} & \beta_{4,i}K_{up} & \beta_{5,i}K_{ua}\\ \beta_{6,i}K_{pu} & \beta_{7,i}K_{pp} & 0\\ \beta_{8,i}K_{au} & 0 & \beta_{9,i}K_{aa}\end{bmatrix}\begin{bmatrix}\boldsymbol{R}_i^u\\ \boldsymbol{R}_i^v\\ \boldsymbol{R}_i^a\end{bmatrix} \quad (32)$$

with

$$\beta_{1,k}=\int_{\omega_{min}}^{\omega_{max}} S_n^{u*}(\omega).S_k^u(\omega)d\omega,\ \beta_{2,k}=\int_{\omega_{min}}^{\omega_{max}}\omega^2 S_n^{u*}(\omega).S_k^u(\omega)d\omega,$$

$$\beta_{3,k}=\int_{\omega_{min}}^{\omega_{max}} j\omega S_n^{u*}(\omega).S_k^u(\omega)d\omega,\ \beta_{4,k}=\int_{\omega_{min}}^{\omega_{max}} S_n^{u*}(\omega).S_k^v(\omega)d\omega,$$

$$\beta_{5,k}=\int_{\omega_{min}}^{\omega_{max}} S_n^{u*}(\omega).S_k^a(\omega)d\omega,\ \beta_{6,k}=\int_{\omega_{min}}^{\omega_{max}} S_k^{u*}(\omega).S_n^a(\omega)d\omega$$

$$\beta_{7,k}=\int_{\omega_{min}}^{\omega_{max}} S_n^{v*}(\omega).S_k^v(\omega)d\omega,\ \beta_{8,k}=\int_{\omega_{min}}^{\omega_{max}} S_k^{a*}(\omega).S_n^u(\omega)d\omega,$$

$$\beta_{9,k}=\int_{\omega_{min}}^{\omega_{max}} S_n^{a*}(\omega).S_k^a(\omega)d\omega,\ \beta_s=\int_{\omega_{min}}^{\omega_{max}} S_k^{a*}(\omega)d\omega,$$

for $k=\{1....n\}$

Where $X^*(\omega)$ denote the conjugated of $X(\omega)$ and $\boldsymbol{F}_a$ the vector source introduced by the imposed boundary condition on the magnetic potential (Fig. 12). We can note that the structure of the previous system is similar to this one presented by (8). The difference is the introduction of coefficients associated with each submatrices.

In a second step, we assume that the functions $R_n^v(\boldsymbol{x})$, $R_n^a(\boldsymbol{x})$ and $\boldsymbol{R}_n^u(\boldsymbol{x})$ are known. Then, the test functions in equations (26), (27) and (28) are $v'=R^v(\boldsymbol{x})S_n^{v'}(\omega)$, $a'=R^a(\boldsymbol{x})S_n^{a'}(\omega)$ and $\boldsymbol{u}'=\boldsymbol{R}^u(\boldsymbol{x})S_n^{u'}(\omega)$ with $S^{v'}(\omega)$, $S^{a'}(\omega)$ and $S^{u'}(\omega)$ test functions defined on the same spaces of $S_n^l(\omega)$ with $l=\{v,\ a,\ u\}$ respectively. To compute the functions $S_n^l(\omega)$, it is possible to use strong formulations of (26), (27) and (28). Then, $S_n^l(\omega)$ are solutions of the following equation system:

$$\begin{bmatrix}\gamma_{1,n}-\omega^2\gamma_{2,n}+j\omega\gamma_{3,n} & \gamma_{4,n} & \gamma_{5,n}\\ \gamma_{6,n} & \gamma_{7,n} & 0\\ \gamma_{8,n} & 0 & \gamma_{9,n}\end{bmatrix}\begin{bmatrix}S_n^u(\omega)\\ S_n^v(\omega)\\ S_n^a(\omega)\end{bmatrix}=$$
$$\begin{bmatrix}0\\0\\ \gamma_s\end{bmatrix}+\sum_{i=1}^{n-1}\begin{bmatrix}\gamma_{1,i}-\omega^2\gamma_{2,i}+j\omega\gamma_{3,i} & \gamma_{4,i} & \gamma_{5,i}\\ \gamma_{6,i} & \gamma_{7,i} & 0\\ \gamma_{8,i} & 0 & \gamma_{9,i}\end{bmatrix}\begin{bmatrix}S_i^u(\omega)\\ S_i^v(\omega)\\ S_i^a(\omega)\end{bmatrix}$$

(33)

with

$$\gamma_{1,k}=\boldsymbol{R}_n^{u*}K_{uu}\boldsymbol{R}_k^u,\ \gamma_{2,k}=\boldsymbol{R}_n^u M_{uu}\boldsymbol{R}_k^u,\ \gamma_{3,k}=\boldsymbol{R}_n^{u*}C_{uu}\boldsymbol{R}_k^u,$$
$$\gamma_{4,k}=\boldsymbol{R}_n^{u*}K_{up}\boldsymbol{R}_k^v,\ \gamma_{5,k}=\boldsymbol{R}_n^{u*}K_{ua}\boldsymbol{R}_k^a,\ \gamma_{6,k}=\boldsymbol{R}_n^{v*}K_{pu}\boldsymbol{R}_k^u,$$
$$\gamma_{7,k}=\boldsymbol{R}_n^{v*}K_{pp}\boldsymbol{R}_k^v,\ \gamma_{8,k}=\boldsymbol{R}_n^{a*}K_{au}\boldsymbol{R}_k^u,\ \gamma_{8,k}=\boldsymbol{R}_n^{a*}K_{aa}\boldsymbol{R}_k^a,$$
$$\gamma_s=\boldsymbol{R}_n^{v*}\boldsymbol{F}_a \qquad \text{for } k=\{1....n\}$$

The equation system (33) is solved for different values of ω such that $\omega=\{\omega_1,\ \ldots,\ \omega_N\}$ with N the number of discrete values.

The two steps are repeated until convergence of all functions $R_n^l(\boldsymbol{x})$ and $S_n^l(\omega)$ with $l=\{v,\ a,\ u\}$. The number of modes used to approximate the solutions (29), (30) and (31) is not known a-priori by the user. Then, a criterion can be introduced to stop the enrichment process [17]. For example, this criterion can be based on the norm of the nth mode with respect to the norm of the first mode,

$$\frac{\left\|R_n^l(\boldsymbol{x})S_n^l(\omega)\right\|}{\left\|R_1^l(\boldsymbol{x})S_1^l(\omega)\right\|}<\varepsilon \text{ for } l=\{v,a,u\} \quad (34)$$

with ε a given value by the user. Other error estimators based on quantities of interest can be developed. For a magnetoelectric problem, the voltage between two electrodes or the maximal deformation evaluated for two successive iterations of the enrichement process could be used as error estimator.

The convergence of the enrichment process can be improved by introducing an update step of the frequency functions after each calculation of the new mode [19]. Then, after the computation of the nth mode, the update stage consists in recomputing the functions $S_j^l(\omega)$ for $j\in[1{:}n]$ with $l=\{v,\ a,\ u\}$ with respect to the functions $R_j^l(\omega)$ $j\in[1{:}n]$.

B. Application

In term of application, we consider the device presented in section V without resistive load. The 2D mesh is composed of 3283 nodes and 6525 triangles. The frequency interval of simulation is fixed at $[10^4;10^5]$Hz with 401 equidistributed discrete values. The PGD method presented in the previous section is applied to obtain approximated solutions. In order to evaluate the efficiency of the PGD method, the same problem is solved with a "classic" FE model. The results obtained from this numerical model will be considered as the reference results. We denote by the subscript PGD and up_PGD the results obtained from the PGD without and with the update step. In order to evaluate the convergence of the enrichment loop, we consider error estimators based on the interest quantities such as the voltage between the two electrodes and the maximal deformations according to the axis x and y. Two criteria can be defined, the first one ε_i evaluates the relative gap on the interest values between two successive iterations of the enrichment loop and the second one ε_r, the relative error between the PGD approximation versus the reference. Then, we have

$$\varepsilon_i X=\frac{\left\|X_i-X_{i-1}\right\|_2}{\left\|X_i\right\|_2} \quad (35)$$

$$\varepsilon_r X=\frac{\left\|X_{ref}-X_i\right\|_2}{\left\|X_{ref}\right\|_2} \quad (36)$$

with X the interest quantity (i.e. the magnitude V of the voltage, def_x and def_y the maximal deformations along x and y) and i the ith mode.

Figs. 17, 18 and 19 show the evolutions of the error ε_r for the magnitude of the voltage and for the maximal deformations along x and y as functions of the number of modes. For all cases, the convergences of the PGD with the

update step are faster than without this additional step. In the following, we consider only the results obtained from the PGD with the update step. We can observe that the error of the voltage decreases faster than those of the maximal deformations. With a low number of modes, the waveform of the voltage magnitude versus the frequency is close to the reference (Fig. 20), with M=2, the relative error ε_rV is close to 0.1%. To obtain a good approximation of the evolutions of the maximal deformations versus the frequency, the number of modes must be enough important. For our case, with M=13, we obtain a good approximation of the maximal deformations along the axis *x* and *y* versus the frequency. Fig. 21 and 22 present the evolution of the maximal deformations obtained from the PGD for different number of modes. We can observe that the maximal deformations on the high frequencies are captured with a low number of modes. The more the number of modes increases and the more the low frequency maximal deformations are captured by the PGD approximation. Fig. 23 presents the evolutions of the relative gap ε_i on the interest quantities between two successive iterations of the enrichment loop (i.e. the magnitude V of the voltage, def_x and def_y the maximal deformations along *x* and *y*) as functions of the number of modes. For all interest quantities, the convergence is not strictly decreasing. For the maximal deformations, a sudden fluctuation corresponds to a new variation of the maximal deformation captured by the last computed mode.

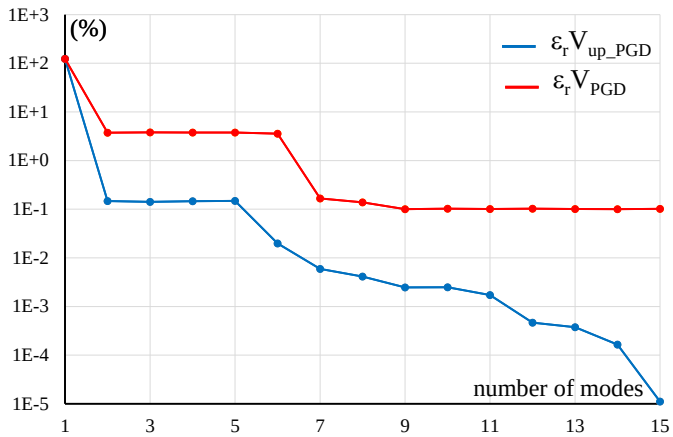

FIG. 17 Relative error of the voltage magnitude as a function of the number of modes

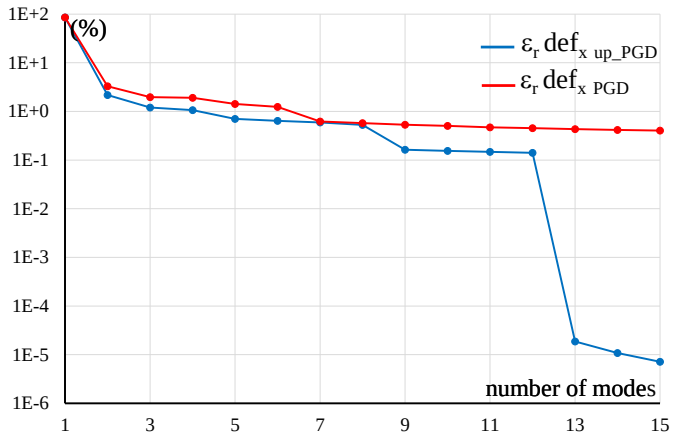

FIG. 18 Error of the maximal deformation along *x* as a function of the number of modes

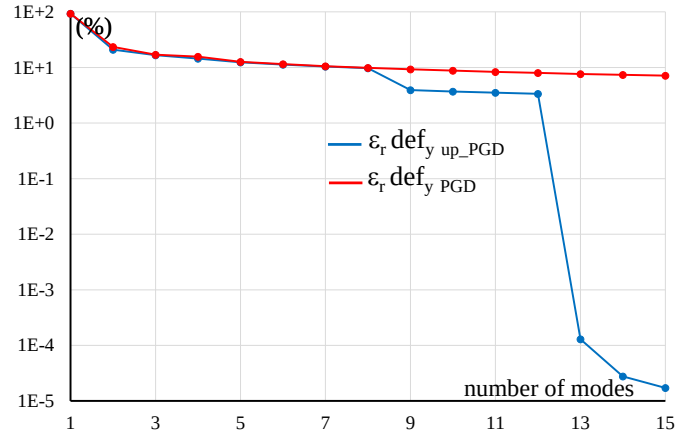

FIG. 19 Error of the maximal deformation along *y* as a function of the number of modes

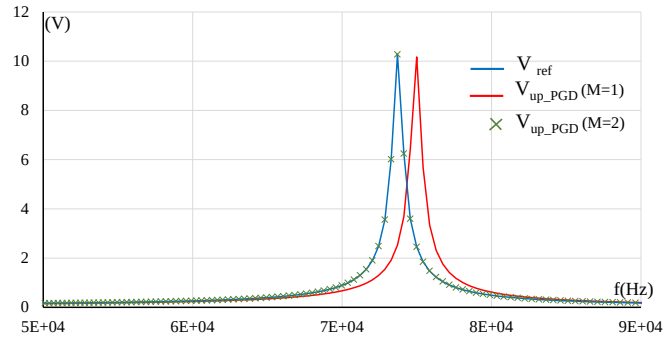

FIG. 20 Magnitude of the voltage versus the frequency

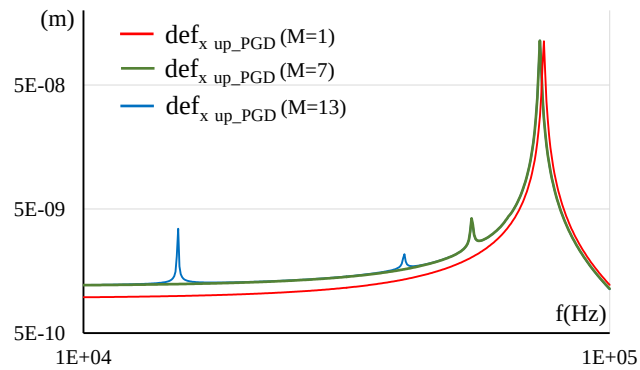

FIG. 21 Maximal deformation along *x* versus the frequency

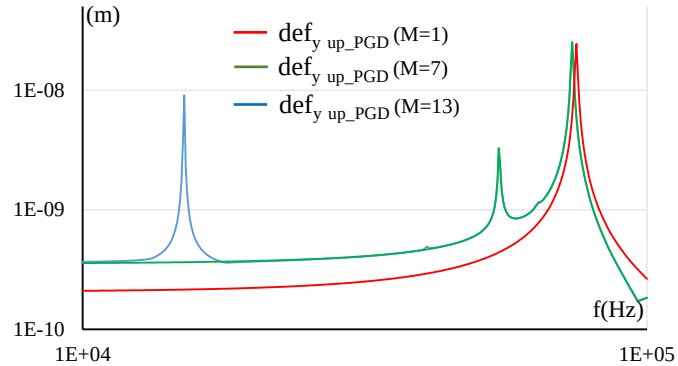

FIG. 22 Maximal deformation along *y* versus the frequency

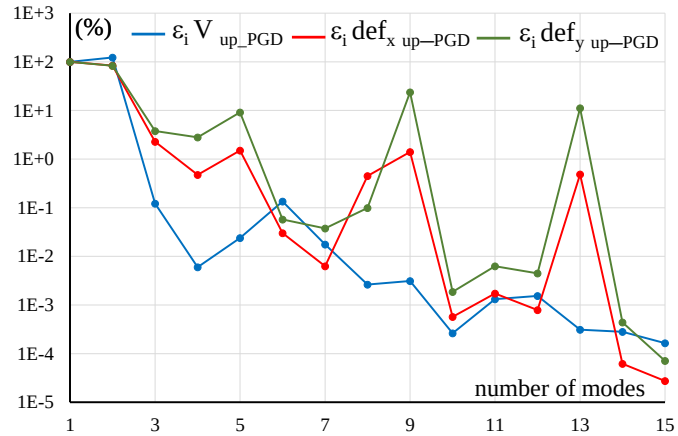

FIG. 23 Relative gaps on the interest values between two successive iterations of the enrichment loop

Fig. 24 illustrates the deformation of the structure at the resonance frequency obtained from the PGD with M=15. From (31), it is possible to present the mechanical deformation associated with each mode. Fig. 25, 26 and 27 present the deformation associated with the first, second and fourth mode. The first and second mode of the mechanical deformation could be illustrated as physical deformations of the structure. For the rest of modes, it is difficult to give a physical sens of the deformations. Fig. 28 present the gap of the deformation at the resonance frequency obtained from the reference and the PGD approximation. The values of the gap distribution are lower compared to the mechanical deformation presented in Fig. 24.

If the interest quantity is the voltage between the two electrodes, the PGD gives a good approximation with M = 2, in this case, the speed up is 34. To obtain mechanical deformations close to the references, the modes number of the PGD solutions must be to 15 modes, the speed up is then 4.3.

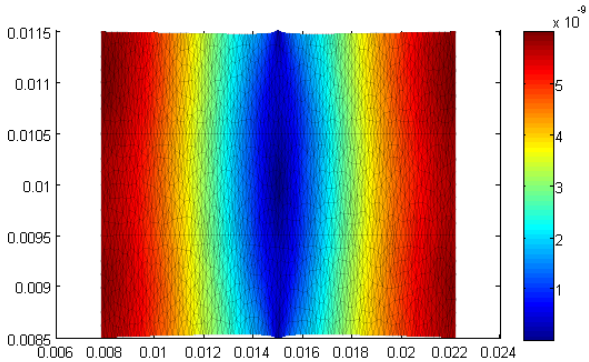

FIG. 24 Deformation of the structure at the resonance frequency obtained from the PGD (M=15)

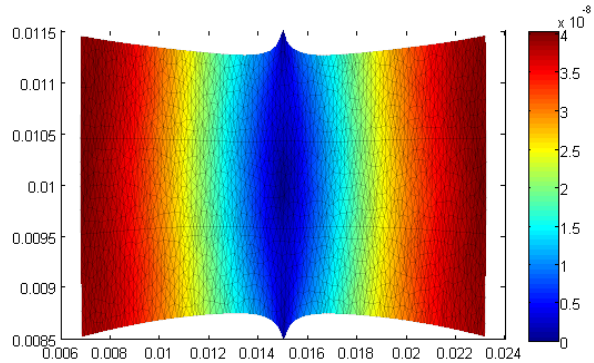

FIG. 25 Deformation of the structure at the resonance frequency for the first mode

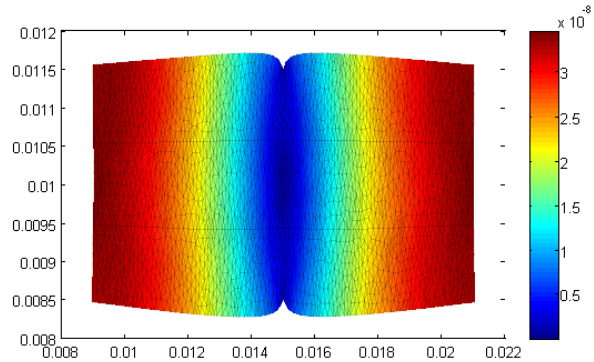

FIG. 26 Deformation of the structure at the resonance frequency for the second mode

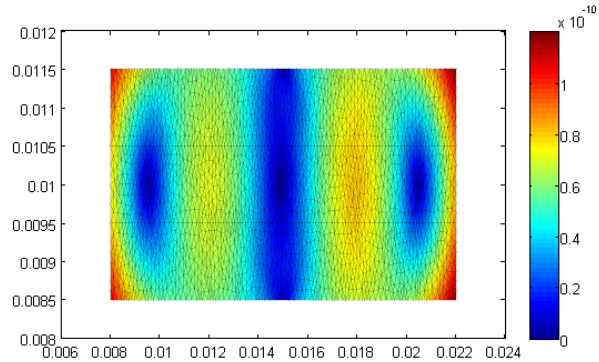

FIG. 27 Deformation of the structure at the resonance frequency for the fourth mode

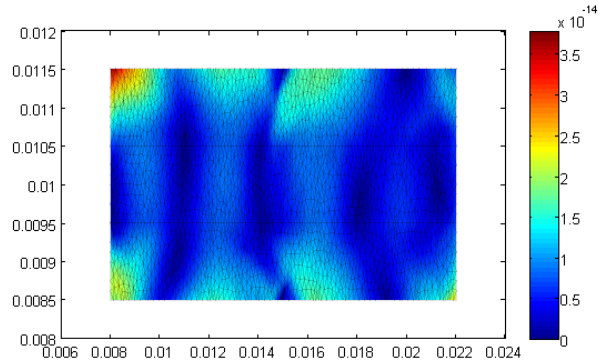

FIG. 28 Gap of the deformation at the resonance frequency obtained from the reference and the PGD approximation

IX. Conclusion

This paper has described the different steps of the establishment of a numerical model applied to the study of magnetoelectric devices. Details on included behavior laws have been presented to introduce the first static and harmonic FE models without consideration of the load. Next, a finite element multiphysics modeling of an energy transducer based on magnetoelectric laminate composites in considering electrical load has been presented. The model has been developed for both harmonic and transient cases and successfully applied to an energy transducer composed of Terfernol-D/PZT/Terfernol-D materials. The harmonic model allows to determine the resonance frequencies and the optimal loads to maximize the deliverable power. The transient model using the Newmark method provides a useful tool to study the energy transfer when a conditioning circuit such as a SSDI harvesting technique is employed. Finally, the PGD method has been developed with the potential formulation used to solve the ME problem. In terms of accuracy, the global quantities such that the voltage can be approximated with a low number of modes and the computation time significantly reduced. If we are interested in local values for the mechanical deformation, a good approximation is obtained with a greater number of modes. Nevertheless, with the studied example, the computation time still remains lower than that obtained from a full model.

References

[1] O. Ouchetto, S. Zouhdi, A. Bossavit, G. Griso, B. Miara, A. Razek, "Homogenization of Structured Electromagnetic Materials and metamaterials", *Journal of Materials Processing Technology*, vol. 181, Issue: 1, 2007.

[2] M. Fiebig, "Revival of the magnetoelectric effect", *Journal Physics D: Applied Physics*, 38:123–152, 2005.

[3] V. E. Wood, A.E. Austin, "Possible applications for magnetoelectric materials", *Int. Journal Magn*. 5, 303-315, 1974.

[4] M. I. Bichurin, V. M. Petrov, S. V. Averkin, E. Liverts, "Present status of theoretical modeling the magnetoelectric effect in magnetostrictive-piezoelectric nanostructures. Part I: Low frequency and electromechanical resonance ranges", *Journal of Applied Physics*, vol 107, 2010.

[5] R. Corcolle, L. Daniel, F. Bouillault, Generic formalism for homogenization of coupled behavior: Application to magnetoelectroelastic behavior, *Physical Review B*, vol. 78, Issue: 0, 2008.

[6] C.-W. Nan, M. I. Bichurin, S. Dong, D. Viehland, G. Srinivasan, "Multiferroic magnetoelectric composites: Historical perspective, status, and future directions", *Journal of Applied Physics*, vol. 103, 2008.

[7] N. Galopin, X. Mininger, F. Bouillault, L. Daniel "Finite Element Modelling of Magnetoelectric Sensors", *IEEE Trans. on Magn.*, vol. 44. no. 6, 2008.

[8] X. Mininger, N. Galopin, Y. Dennemont, F. Bouillault, "3D finite element model for magnetoelectric sensors", *Eur. Phys. J. Appl. Phys*, vol. 52, 2010.

[9] N. Galopin, "Finite Element Modeling of Magnetoelectric Composites with Interdigitated Electrodes", Compumag 2015, Montréal, Canada, 2015.

[10] Y. X. Liu, J. G. Wan, J.-M. Liu, C. W. Nan "Effect of magnetic bias field on magnetoelectric coupling in magnetoelectric composites", *Journal of Applied Physics*, vol. 94, 2003.

[11] T. T. Nguyen, X. Mininger, L. Daniel, F. Bouillault, "Influence of Mechanical Boundary Conditions on Magnetolectric Sensors", *IEEE Trans. on Magn.*, vol. 49. no. 5, 2013.

[12] T. T. Nguyen, F. Bouillault, L. Daniel, X. Mininger, "Finite element modeling of magnetic field sensors based on nonlinear magnetoelectric effect", *Journal of Applied Physics*, vol. 109, 2011.

[13] D. T. Huong Giang, N. H. Duc, "Magnetoelectric sensor for microtesla magnetic-fields based on $(Fe_{80}Co_{20})_{78}Si_{12}B_{10}$/PZT laminates", Sensors and Actuators A: Physical, vol. 149, 2, 2009.

[14] J. Lou, D. Reed, M. Liu, N. X. Sun, "Electrostatically tunable magnetoelectric inductors with large inductance tenability", *Applied Physics Letters*, vol. 94, 2009.

[15] T. Lafont, L. Gimeno, J. Delamare, G. A. Lebedev, D. I. Zakharov, B. Viala, O. Cugat, N. Galopin, L. Garbuio, O. Geoffroy, "Magnetostrictive-piezoelectric composite structures for energy harvesting", *Journal of Micromechanics and Microengineering*, vol. 22, 094009, 2012.

[16] H. Talleb, Z. Ren, J. Jiao, L. Liu, W. Di, H. Luo, S. Wing, "Finite element modeling of magnetoelectric laminate composites in considering nonlinear and load effects for energy harvesting", *Journal of Alloys and Compounds*, vol. 615, pp. 65-74, 2014.

[17] D. Guyomar, A. Badel, E. Lefeuvre, C. Richard, "Toward energy harvesting using active materials and conversion improvement by nonlinear processing", *Ultrasonics, Ferroelectrics and Frequency Control, IEEE Transactions* on, vol. 52, no. 4, pp. 584-595, 2010.

[18] R. Corcolle, E. Salaün, F. Bouillault, Y. Bernard, C. Richard, A. Badel, D. Guyomar, "Modeling of a beam structure with piezoelectric materials: introduction to SSD techniques", *COMPEL*, vol. 27, 1, pp. 205-214, 2008.

[19] H. Talleb, Z.Ren, "Finite Element Modeling of a Magnetoelectric Energy Transducer Including the Load Effect", *IEEE Trans. on Magn*, vol.51, no.3, pp.1-5,

[20] F. Chinesta, R. Keunings and A. Leyguel, *The Proper Generalized Decomposition for Advanced Numerical Simulations*, A. Primer, Springer International Publishing, 2014.

[21] E. Pruliere, F. Chinesta and A. Ammar, "On the deterministic solution of multidimensional parametric models using the Proper Generalized Decomposition", *Numerical Methods in Engineering*, Mathematics and Computers in Simulation, Elsevier, vol. 81 (4), pp.791-810, 2010.

[22] L. Tamellini, O. Le Maître and A. Nouy, "Model Reduction Based on Proper Generalized Decomposition for the Stochastic Steady Incompressible Navier-Stokes Equations", *SIAM J. Sci. Comput.* vol. 36(3), pp. A1089-A1117, 2014.

[23] P. Alotto, M. Guarnieri, F. Moro, A. Stella "A proper generalized decomposition approach for modeling fuel cell polymeric membranes" *IEEE Trans. Mag.*, vol. 47(5), pp. 1462–1465, 2011.

[24] T. Henneron, A. Benabou, S. Clénet, "Nonlinear Proper Generalized Decomposition Method Applied to the Magnetic Simulation of a SMC Microstructure", *IEEE Trans. Mag.*, vol. 48(11), pp. 3242-3245, 2012.

[25] T. Henneron and S.Clénet, "Application of the PGD and DEIM to Solve a 3-D Non-Linear Magnetostatic Problem Coupled With the Circuit Equations", IEEE Trans. Magn., vol. 52, no. 3, pp. 7202104, 2016.

[26] M. Pineda-Sanchez et al., "Simulation of skin effect via separated representations", *COMPEL*, vol. 29(4), pp.919 – 929, 2010.

[27] T. Henneron, S. Clénet, "Model order reduction of quasi-static problems based on POD and PGD approaches", *Eur. Phys. J. Appl. Phys.*, vol. 64(2), 24514, 7 pages, 2013.

[28] T. Henneron and S.Clénet, "Proper generalized decomposition method applied to solve 3D magnetoquasi-static field problems coupling with external electric circuits", IEEE Trans. Magn., vol. 51, no. 6, pp. 7208910, 2015.

[29] Z. Qin, H.Talleb and Z..Ren, "A proper generalized decomposition based solver for nonlinear magneto-thermal problems", *IEEE Trans. Magn.*, vol. 52, no. 2, pp. 7400209, 2016.

[30] Z. Qin, H. Talleb, S.Yan,and Z..Ren, "Application of the PGD in Parametric Finite Element Simulation of a Piezoelectric Energy Harvester", 10th International Symposium on Electric and Magnetic Fields (EMF 2016), (Lyon) France, 2016.

Authors name and affiliation

Xavier Mininger, Group of electrical engineering-Paris, CNRS UMR8507, CentraleSupelec, Univ Paris Sud, UPMC, 11 rue Joliot Curie, Plateau de Moulon, 91192 Gif sur Yvette Cedex,

France, Tel. +33169851658,
xavier.mininger@geeps.centralesupelec.fr
Hakeim Talleb, Sorbonne Universités, UPMC Univ Paris 06, UR2, L2E, F-75005, Paris, France, Tel. +33144274310, hakeim.talleb@upmc.fr
Thomas Henneron, Université Lille1, Laboratory of electrical engineering and power electronics (L2EP), EA 2697, bat. P2, cité scientifique, 59655 Villeneuve d'ascq, France, Tel. +3320434865, thomas.henneron@univ-lille1.fr

The authors are from the organizing laboratories of Compumag 2019.